Geophysical Research Letters

Key Points:
- We exploit spectral characteristics of sea surface height (SSH) to partition ocean motions into balanced motions and internal gravity waves
- We use a simple shallow-water model to diagnose internal gravity wave motions from SSH
- We test a dynamical framework to recover the interactions between internal gravity waves and balanced motions from SSH

Correspondence to:
H. S. Torres,
hector.torres.gutierrez@jpl.nasa.gov

Diagnosing Ocean-Wave-Turbulence Interactions From Space

H. S. Torres[1] [ID], P. Klein[1,2] [ID], L. Siegelman[1,3] [ID], B. Qiu[4] [ID], S. Chen[4] [ID], C. Ubelmann[5], J. Wang[1] [ID], D. Menemenlis[1] [ID], and L.-L. Fu[1] [ID]

[1]Jet Propulsion Laboratory, California Institute of Technology, Pasadena, CA, USA, [2]LOPS/IFREMER, Plouzane, France, [3]LEMAR, Plouzane, France, [4]Department of Oceanography, University of Hawaii at Manoa, Honolulu, HI, USA, [5]Collecte Localisation Satellites, Ramonville St-Agne, France

Abstract Numerical studies indicate that interactions between ocean internal gravity waves (especially those <100 km) and geostrophic (or balanced) motions associated with mesoscale eddy turbulence (involving eddies of 100–300 km) impact the ocean's kinetic energy budget and therefore its circulation. Results from these studies have never been confirmed by observations in regional or basin-scale domains. Here we show that internal gravity waves have a spectral signature on sea surface height during summer that significantly differs from that of balanced motions. These spectral differences lead us to propose a new dynamical framework that quantifies the interactions between internal gravity waves and balanced motions in physical space from sea surface height snapshots, and in particular the energy exchanges between them. Our results, using this dynamical framework, highlight the strong potential of future satellite altimeter missions to make critical advances in assessing the ocean's kinetic energy budget from observations in large domains.

1. Introduction

Two classes of motions dominate ocean kinetic energy (KE): balanced motions (BMs) and internal gravity waves (IGWs). BMs considered in this study involve motions associated with mesoscale eddy turbulence, such as mesoscale eddies (with a 100- to 300-km size) and also smaller-scale structures with horizontal scales down to 10 km (Ferrari & Wunsch, 2009). BMs are principally in geostrophic balance (balance between pressure forces and Coriolis forces), with their frequencies smaller than or close to the Coriolis frequency, f. They are mostly energetic in turbulent regions such as the Gulf Stream, the Kuroshio Extension, and the Antarctic Circumpolar Current. BMs account for almost 80% of the total ocean KE and explain most of the advective horizontal and vertical transport of heat and any tracers (Ferrari & Wunsch, 2009). IGWs, on the other hand, are waves with frequencies close to or larger than f and spatial scales from hundreds of kilometers to tens of meters. Unlike BMs, IGWs are weakly nonlinear and characterized by a fast propagation (Alford et al., 2016). They include coherent internal tides, wind-driven near-inertial waves, and an IGW continuum with higher frequencies and much smaller spatial scales than the coherent internal tides and near-inertial waves. In turbulent regions, KE at scales larger than 100 km is principally dominated by BMs (Ferrari & Wunsch, 2009). KE at smaller scales is usually dominated by BMs in winter and IGWs in summer (Callies et al., 2015; Qiu et al., 2018; Rocha, Gille, et al., 2016; Torres et al., 2018).

The motivation for partitioning motions into BMs and IGWs is that they impact the ocean KE budget differently (Klein et al., 2019). BMs mostly experience an inverse KE cascade, with KE fluxing from sources (starting from ~30- to 50-km wavelength) toward larger scales, which contributes to sustain mesoscale eddy turbulence (Arbic et al., 2012; Qiu et al., 2014; Sasaki et al., 2014). IGWs, on the other hand, and in particular the IGW continuum, experience a direct KE cascade with KE fluxing toward smaller scales, ultimately leading to irreversible mixing (Polzin & Lvov, 2011). As such, IGWs map out an important path in the route to KE dissipation that affects mesoscale eddy turbulence.

However, BMs and IGWs do not evolve independently but strongly interact, and their interaction further impacts the ocean KE budget. Numerous studies, starting with Kunze (1985) and Young and Jelloul (1997), have shown that IGWs at large scales are scattered and dispersed by mesoscale eddies, leading to waves with smaller spatial scales and higher frequencies, trapped within anticyclonic eddies and expelled from cyclonic ones (Danioux et al., 2008; Whitt & Thomas, 2015). More recent theoretical and numerical
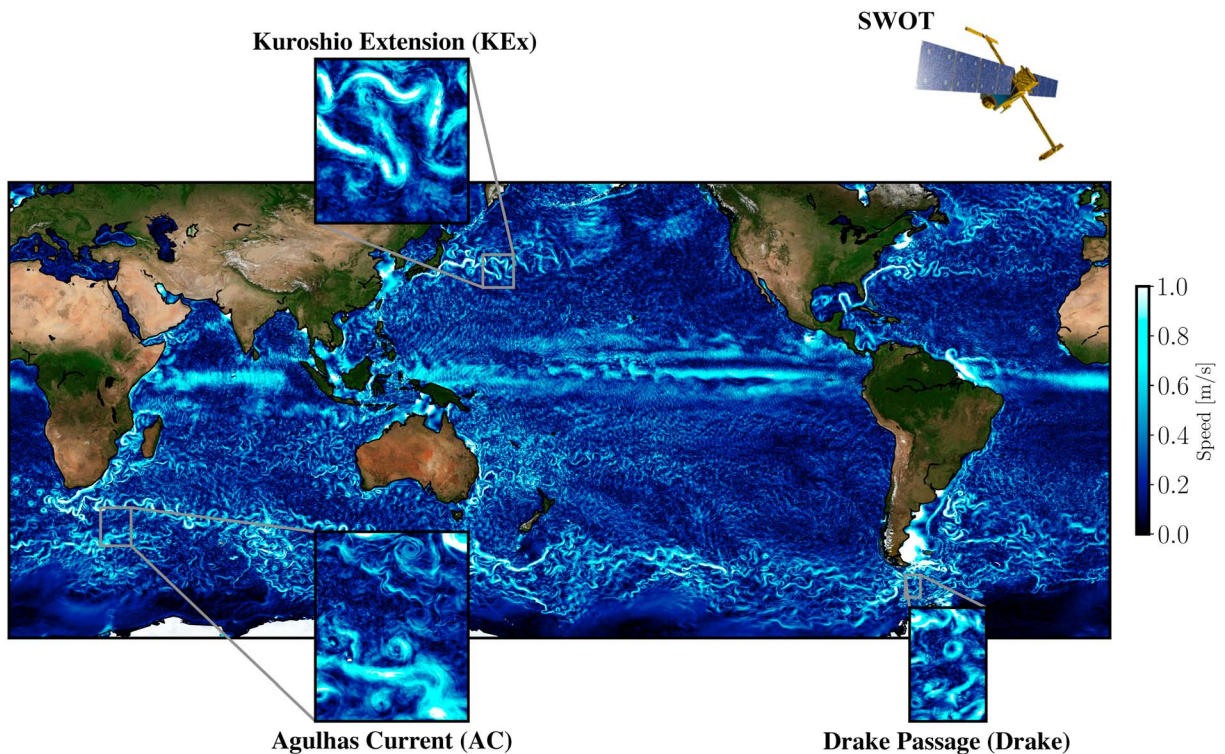
Figure 1. Map of surface speed in the world ocean from the OGCM (see Methods, section A). The zooms correspond to the three regions considered in this study, namely the Kuroshio-Extension [KEx, 30°N, 156°E],) the Agulhas Current [AC, 40°S, 30°E] and the Drake Passage [Drake, 62°S, 67°W].

studies emphasize that these scattering mechanisms facilitate the energy exchanges between BMs and IGWs, exacerbating the cyclone-anticyclone asymmetry and eventually further dissipating mesoscale eddies (Barkan et al., 2017; Rocha et al., 2018; Taylor & Straub, 2016; Thomas, 2017). These theoretical and numerical results have never been confirmed by in situ and/or space observations in regional or basin-scale domains.

The present study addresses this observational challenge in the context of the upcoming Surface Water and Ocean Topography satellite mission, SWOT (Fu & Ferrari, 2008). Starting in 2021, SWOT will provide observations of the SSH, interpreted as a stream function or surface pressure, with unprecedented spatial resolution (up to ~10 km) on a global scale. In the meantime, to assess the potential of these observations, our study uses as a testbed the numerical outputs of an ocean global circulation model (OGCM), tidal resolving and with a very high-resolution (1/48° in the horizontal and 90 vertical levels) (see section A in supporting information for a detailed description of the model). Our results indicate that SSH observations at high resolution can be used to monitor the BM-IGW interactions and in particular the energy exchanges between BMs and IGWs, making a critical advance in assessing the potential for monitoring the KE budget of the world's oceans from space.

Our study exploits one SSH characteristic pointed out in Rocha, Chereskin, et al. (2016) and subsequent studies [see Torres et al., 2018, and references herein]: The SSH wave number spectrum displays, in summer, a significant slope discontinuity at a scale in the 50- to100-km range. The shallower spectral slope at smaller scales within that range is explained by IGWs and the steeper slope at larger scales by BMs (Qiu et al., 2018; Torres et al., 2018). This SSH characteristic motivated us to develop a dynamical framework to diagnose BMs and IGWs directly from SSH snapshots and to recover the IGW-BM energy exchanges. We focus on three energetic regions during summer (Figure 1), namely, the Kuroshio Extension (August-September-October), the Agulhas Current (January-February-March), and the Drake Passage (January-February-March). The dynamical framework and the resulting diagnosis method are detailed in section 2 (see also section B in supporting information). The diagnosis method is then tested in section 3. Results illustrate the performance to recover from SSH snapshots, not only IGWs and BMs in physical space but also the KE exchanges between BMs and IGWs. Although our study is a first attempt, these results emphasize the
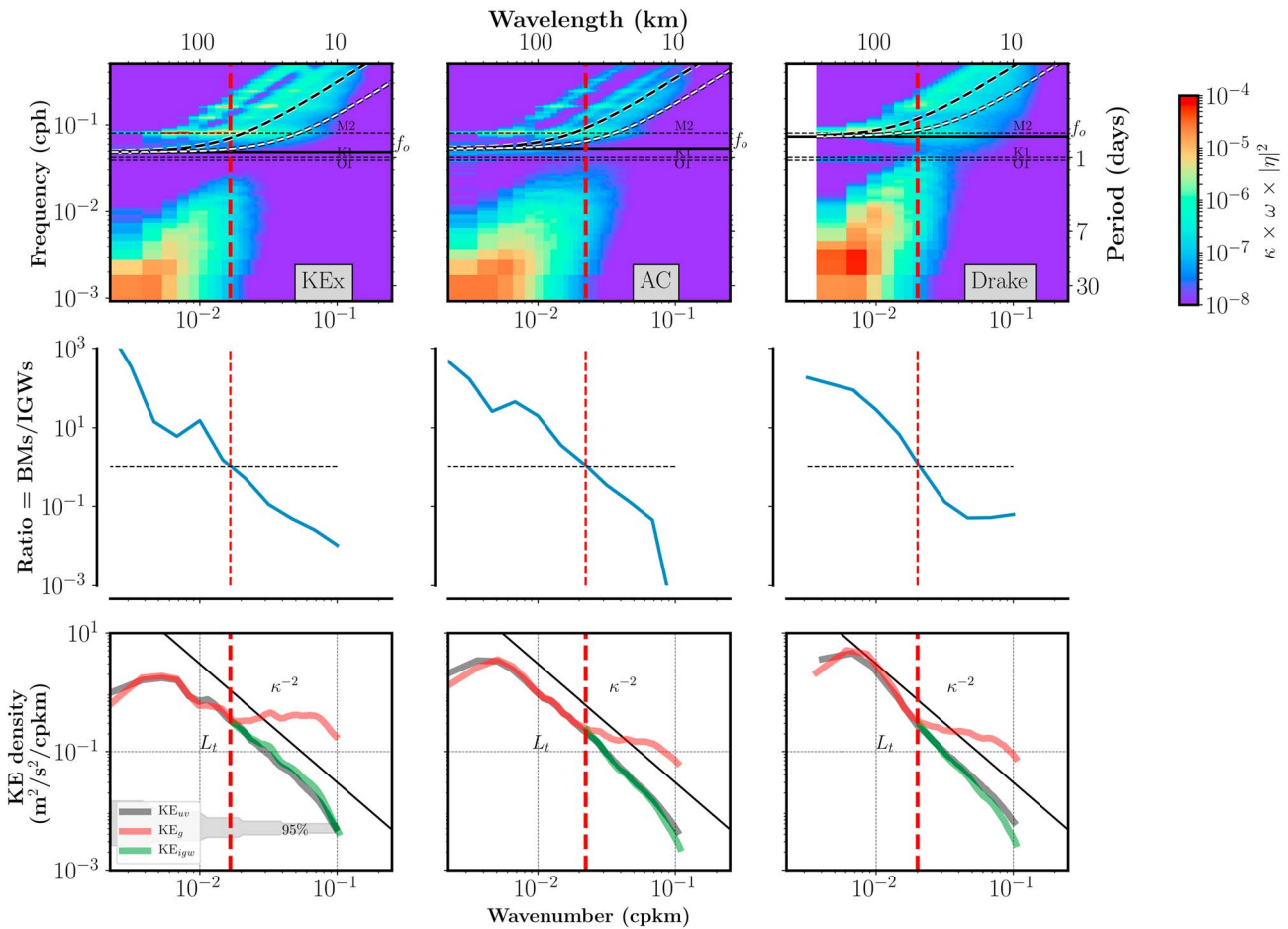
Figure 2. (top panels) The $\omega - \kappa$ spectra of sea surface height (SSH) from the ocean global circulation model (see Methods) for the three targeted regions. The white (black) thick dashed curve stands for the dispersion relation of internal gravity waves for baroclinic mode-10 (mode-3). The red dashed lines mark the transition $Lt = K_i^{-1}$ between BMs and IGWs dominance. (middle panels) Ratio $[R(\kappa)]$ between BMs and IGWs variances as a function of wave number, κ. (bottom panels) KE_g (red lines): Geostrophic kinetic energy spectra diagnosed (using B3) from the SSH wave number spectra (estimated from the $\omega - \kappa$ spectra integrated over all frequencies), KE_{uv} (gray lines): Kinetic energy spectra deduced from u and v, and KE_{igw} (green lines): internal gravity wave kinetic energy diagnosed from SSH (using B8). From left to right, each panel refers, respectively, to the Kuroshio-Extension [KEx, 30°N, 156°E],) the Agulhas Current [AC, 40°S, 30°E] and the Drake Passage [Drake, 62°S, 67°W]. IGWs = internal gravity waves; BMs = balanced motions; KE = kinetic energy.

unexpected strong potential of future wide-swath satellite altimeters to monitor BM-IGW interactions from SSH in energetic oceanic regions. The last section discusses the caveats related to our framework.

2. A Dynamical Framework to Diagnose IGWs and BMs From SSH

2.1. Partitioning BMs and IGWs in Spectral Space

One approach to partition motions into BMs and IGWs, using numerical outputs from an OGCM(see section A in supporting information), is to move to the frequency (ω)-wave number (κ) domain. Indeed, as explained in Qiu et al. (2018) and Torres et al. (2018), the dispersion relation curve associated with the highest baroclinic mode taken into account in the model (the 10th baroclinic mode in the model we use, see dashed white line in Figure 2, top panels) separates IGWs located above this curve and the BMs located below (Figure 2, top panels). A more quantitative approach to infer the dominance of BMs over IGWs is to calculate for each wave number the ratio between the SSH variance below the dashed white line (i.e., BMs) and SSH variance above this line (i.e., IGWs) [Qiu et al., 2018 and Torres et al., 2018]. This ratio, $R(\kappa) = BM_{variance}/IGW_{variance}$, plotted on Figure 2 (middle panels), highlights the existence of a wave number, K_i (red dashed lines on Figure 2), that clearly separates the region with smaller wave numbers where BMs dominate (with $R(\kappa) \gg 1$) from the one with larger wave numbers where IGWs dominate (with $R(\kappa) \ll 1$). The wave number,

K_i, corresponds to wavelengths close to 55, 50, and 40 km, respectively, for the Kuroshio Extension, the Agulhas Current, and the Drake Passage.

2.2. Spectral Relationships Between SSH Variance and KE for BMs and IGWs

Oceanic observations do not give access to a full $\omega - \kappa$ spectrum. They give access only to either a frequency spectrum (as mooring observations) or a wave number spectrum (as SSH observations). The present study makes use of SSH observations and in particular exploits a conspicuous property of the SSH wave number spectrum in summer. It concerns a significant spectral slope discontinuity between a steep slope (in a κ^{-4} − κ^{-5}) for small wave numbers and a shallower slope (in a κ^{-2}) for larger wave numbers (Rocha, Chereskin, et al., 2016, Torres et al., 2018). Integration of the $\omega - \kappa$ spectra of Figure 2 (top panels) over all frequencies reveals, in each region, an SSH wave number spectrum (not shown) with such a spectral slope discontinuity at exactly the same wave number, K_i, as the one revealed by the ratio, $R(\kappa)$. To further check whether this spectral slope discontinuity allows to partition motions into BMs and IGWs, we have diagnosed the KE from SSH using the classical relationship between SSH and BMs and using an appropriate relationship between SSH and IGWs motions (see section B in supporting information for details). The diagnosed KE spectra are then compared with the one deduced from surface motions.

If we apply the classical relationship between SSH and BMs (that makes use of the geostrophic balance) to the full SSH spectrum, we get the red curves (KE_g-spectra) displayed in Figure 2 (bottom panels). These curves exhibit in all regions a slope discontinuity at the same wave number as the one revealed by the ratio $R(\kappa)$, that is, $\kappa = K_i$. Compared with the KE spectrum estimated from surface motions (i.e., KE_{uv}, gray curves in Figure 2, bottom panels), there is a quantitative agreement in the three regions for $\kappa < K_i$, which validates the geostrophic approximation. However, for $\kappa > K_i$, a breakdown of the geostrophic balance is observed since KE_g-spectra display a flat slope in this scale range, whereas KE_{uv}-spectra have still a κ^{-2} spectral slope.

We now choose an appropriate relationship between SSH and IGW motions for the wave number range $\kappa > K_i$. As detailed in the section B in supporting information, this relationship (equation B8 in supporting information) is based on a simple linear shallow-water model (LSWM). Choosing such a model assumes that the largest part of the IGWs is captured by only one baroclinic mode. Using matching conditions to guarantee the continuity of the SSH and KE spectra at $\kappa = K_i$ (see section B in supporting information), we have found that this baroclinic mode is directly related to the wave number K_i and is very close to the third baroclinic mode for the three regions (black dashed curves on top panels in Figure 2). The KE_{igw}-spectra diagnosed from SSH using this relationship, shown by the green lines in Figure 2 (bottom panels), are very close to the KE_{uv} spectra in the three regions.

The good correspondence between the KE_g spectra (for $\kappa < K_i$) and the KE_{igw} spectra (for $\kappa > K_i$) with the KE_{uv} spectra in the three regions indicates that the slope discontinuity in the SSH wave number spectrum in summer clearly separates IGWs at small scales from BMs at larger scales. More importantly, our approach indicates that the wave number corresponding to this discontinuity further identifies the baroclinic mode that captures the largest part of the IGWs, leading to an adequate relationship between SSH and IGW motions in summer.

2.3. A Methodology to Diagnose Separately BMs and IGWs in Physical Space

The success of the approach described in the preceding section—using the geostrophic approximation for BMs and a single LSWM for IGWs to retrieve the full KE spectrum from a seasonal SSH spectrum—opens the possibility to diagnose the two-dimensional surface velocity field of both BMs and of IGWs in physical space from two-dimensional SSH snapshots.

To test this possibility, the following methodology is used. We consider a single snapshot of the SSH field, $\eta(x,y)$. We define a domain with double periodic conditions by multiplying $\eta(x,y)$ by a two-dimensional Hanning window (see section C in supporting information) and, then, we apply a two-dimensional Fourier transform to the resulting $\eta(x,y)$ field to get $\widehat{\eta}(k,l)$, where the symbol ^ refers to the Fourier transform and k and l the wave number components. This field is partitioned as follows: $\widehat{\eta}(k,l) = \widehat{\eta}_g(k,l)\big|_{\kappa^2=k^2+l^2<K_i^2} + \widehat{\eta}_{igw}\big|_{\kappa^2=k^2+l^2>K_i^2}$ (see section

B in supporting information). Next, we diagnose BMs and IGWs in the spectral space using the appropriate relationships for BM and IGW motions (relations B2 and B7 in section B in supporting information). Finally, we recover BMs and IGWs in physical space using an inverse Fourier transform.
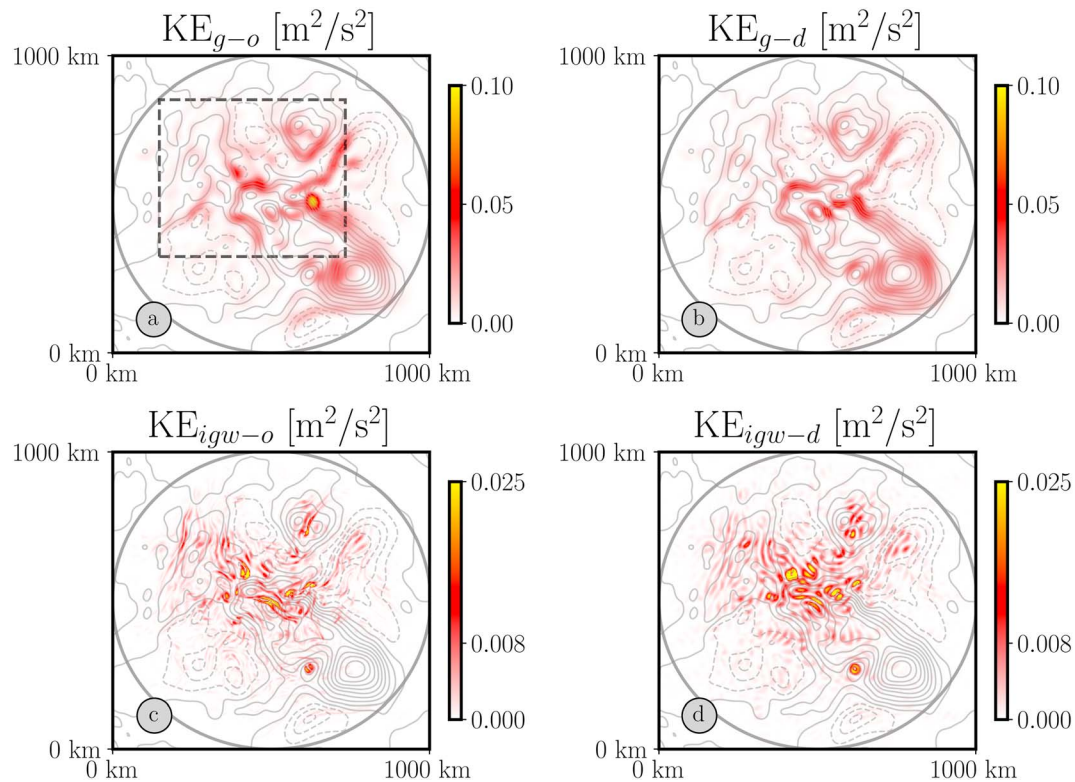
Figure 3. Two-dimensional kinetic energy field for the Kuroshio Extension. Top panels, (a) mesoscale kinetic energy, KE$_{g-o}$ deduced from u and v, (c) internal gravity wave kinetic energy KE$_{igw-o}$ deduced from u and v. Bottom panels, (b) geostrophic kinetic energy, KE$_{g-d}$ diagnosed from sea surface height (SSH) and (d) internal gravity wave kinetic energy KE$_{igw-d}$ diagnosed from SSH. The light gray lines stand for SSH contours. Note that for a pointwise comparison with the diagnosed fields, $u(x,y)$ and $v(x,y)$ have been multiplied by a two-dimensional Hanning window before estimating the observed KE, that is, KE$_{g-o}$ and KE$_{igw-o}$ The gray circle delineates the region of influence of the Hanning window. Correlation between KE$_{g-o}$ and KE$_{g-d}$ is 0.9 and 0.7 between KE$_{igwO}$ and KE$_I$. KE = kinetic energy; IGWs = internal gravity waves.

3. Results

3.1. Diagnosing BMs and IGWs in Physical Space

We test the preceding methodology using our numerical simulation (section A in supporting information). We consider a two-dimensional SSH snapshot [i.e., $\eta(x,y)$], extracted from the numerical simulation outputs. Then, we diagnose separately BMs and IGWs in physical space using the methodology described before. Results, in terms of the KE explained by BMs (KE$_{g-d}$) and IGWs (KE$_{igw-d}$) with subscript d for diagnosed, are shown in Figures 3b and 3d for the Kuroshio Extension (see also Figures S2 and S3 in the supporting information, respectively, for the Agulhas Current and the Drake Passage). Note that the color bar for BMs is 4 times larger than that for IGWs. BMs have larger spatial scales than IGWs, as expected. We compare these diagnosed KE fields with those observed in the OGCM, that is, KE$_{g-o}$ and KE$_{igw-o}$ (with subscript o for observed), in Figures 3a and 3c, respectively (see also Figures S2 and S3). KE$_{g-o}$ and KE$_{igw-o}$ are estimated from $u(x,y)$ and $v(x,y)$ using high-pass and low-pass filters involving K_i^{-1}.

Comparison between Figures 3a and 3b indicates a strong similarity between KE$_{g-o}$ and KE$_{g-d}$. For the Kuroshio Extension, the mean value for KE$_{g-d}$ is close to 0.056 m^2/s^2, consistent with KE$_{g-o}$ value, 0.055 m^2/s^2. Similar results are found for other regions. The KE$_{g-o}$ and KE$_{g-d}$ fields display smooth patterns intensified on the eddy edges (identified by SSH contours). Peaks in the KE$_{g-d}$ field are at the same location as those in the KE$_{g-o}$ field, with the same intensity. This similitude is confirmed by a pointwise comparison that leads to a correlation between KE$_{g-d}$ and KE$_{g-o}$ of 0.9, 0.87, and 0.85, respectively, for the Kuroshio Extension, the Agulhas Current, and the Drake Passage. Comparison of the velocity vectors observed in the simulation with the one diagnosed from SSH (first row in Figure 4, see also Figures S4 and S5) is quite good, as expected, except in the Drake Passage (Figure S5 where BMs might be in gradient wind balance (Vallis, 2017) instead of geostrophic balance.
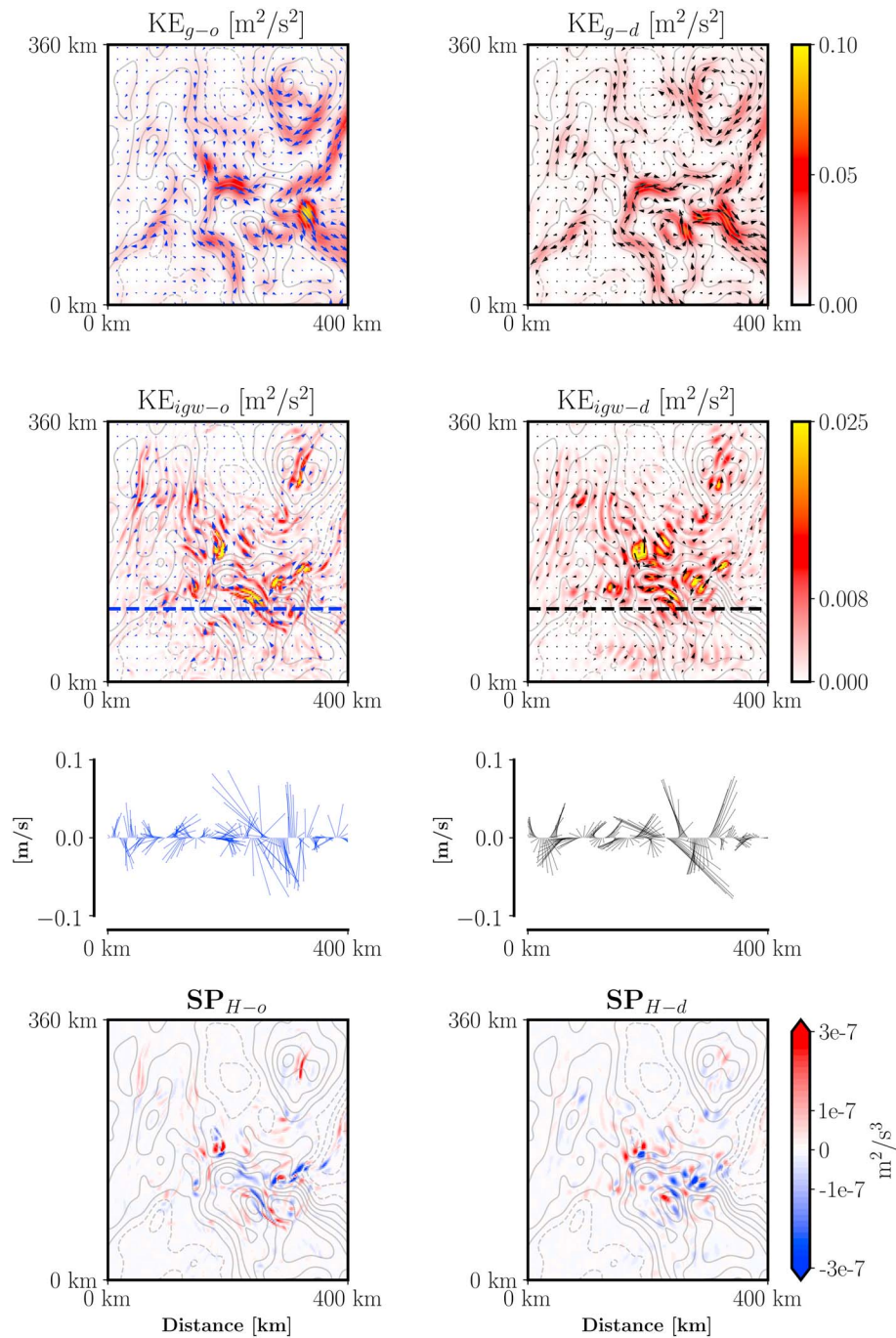
AGU
100
ADVANCING EARTH
AND SPACE SCIENCE

Geophysical Research Letters

10.1029/2019GL083675

Figure 4. Zooms of the two-dimensional kinetic energy field and velocity vectors for the Kuroshio Extension. From top to bottom: first row; (left) mesoscale kinetic energy, KE_{g-o} deduced from u and v; right) geostrophic kinetic energy KE_{g-d} diagnosed from sea surface height (SSH). Second row; (left) Internal gravity wave kinetic energy, KE_{igw-o}, deduced from u and v; right) internal gravity wave kinetic energy, KE_{igw-d}, diagnosed from SSH. The light gray lines stand for SSH contours. Third row; stick diagram of velocity vector for IGWs corresponding to the dashed lines displayed in the middle panels. Fourth row; Kinetic energy exchange between BMs and IGWs by the shear production term, SP (see equation (1)), in the Kuroshio Extension: deduced from u and v (SP_{H-o}, left panel) and diagnosed from SSH (SP_{H-d}, right panel). Correlation coefficient between SP_{H-o} and SP_{H-d} is 0.45. The mean value of the shear production estimated from u and v is -1.17×10^{-9} m^2/s^3 and the mean value of the shear production estimated from SSH is -2.5×10^{-9} m^2/s^3.

Next, we compare IGWs observed in the simulation with those diagnosed from SSH (see panels c [KE_{igw-o}] and d [KE_{igw-d}] in Figures 3, S2, and S3). A first comment is that KE_{igw-o} patterns differ much from KE_{g-o} patterns. Besides having smaller scales, their locations and geometries totally differ. IGW patterns are often located not only on the eddy edges but also inside the eddies (as in the Drake Passage, Figure S3). Sometimes,

they look like radial patterns on the eddy edges as in the Agulhas Current region (Figure S2), a reminder of some recent studies (see Figure 3 in Rocha et al., 2018). The Root-Mean-Square (RMS) value of the $KE_{igw\text{-}d}$ field (0.025 m^2/s^2) is close to the one for $KE_{igw\text{-}o}$ (0.024 m^2/s^2). Similar results are found in other regions (Figures S2 and S3). $KE_{igw\text{-}d}$ is intensified at the same locations as $KE_{igw\text{-}o}$, although this intensification seems to be larger in the $KE_{igw\text{-}d}$ field. The geometry of the $KE_{igw\text{-}d}$ patterns is quite similar to $KE_{igw\text{-}o}$ patterns. Scales of $KE_{igw\text{-}d}$ are slightly larger than those observed in the simulation. The correlation value between $KE_{igw\text{-}o}$ and $KE_{igw\text{-}d}$ is 0.7 instead of 0.9 for the BM fields. Lower correlations are found for other regions (0.66 and 0.48, respectively, for the Agulhas Current and the Drake Passage). However, considering that $KE_{igw\text{-}o}$ has a magnitude lower than $KE_{g\text{-}o}$ and IGW scales are smaller than BM scales, even such a moderate correlation is encouraging. Finally, we compare the IGW velocity vectors observed in the simulation with those diagnosed from SSH (see second row in Figures 4, S4, and S5). Again, the resemblance between the two fields, in terms of magnitude and direction, is remarkable, although not as good as for BMs. For a better comparison, we have plotted two zonal sections of the IGW velocity vectors (third row in Figures 4, S4, and S5). The amplitudes and directions of these vectors compare well in the Kuroshio Extension and in the Agulhas Current, but not as well in the Drake Passage. IGW velocity vectors are often aligned with the $KE_{igw\text{-}o}$ or $KE_{igw\text{-}d}$ patterns, in particular, when these patterns are radial with respect to eddies. This alignment suggests an energy exchange between BMs and IGWs (Thomas, 2017).

3.2. Recovering BM–IGW Interactions From Space

BM-IGW interactions might lead to significant energy exchanges between these two classes of motions (Barkan et al., 2017; Rocha et al., 2018; Taylor & Straub, 2016; Thomas, 2017). The results of the previous section have encouraged us to test the possibility of inferring these exchanges from SSH observations. One quantity we have considered is the KE exchange between BMs and IGWs. From the KE equation (see, e.g., Barkan et al., 2017), the expression of this term (the shear production term, or SP_H) is

$$SP_H = -\left[u_{igw}^2 - v_{igw}^2\right]\frac{\partial U_g}{\partial x} + u_{igw}v_{igw}\left[\frac{\partial V_g}{\partial x} + \frac{\partial U_g}{\partial y}\right]. \tag{1}$$

A positive (negative) SP_H value means a KE transfer from BMs (IGWs) to IGWs (BMs). We have estimated SP_H using the velocity field from the numerical outputs (Figure 4, first and second rows, left panels) and the one diagnosed from SSH (Figure 4, first and second rows, right panels). For the Kuroshio Extension region, the resulting fields $SP_{H\text{-}o}$ (observed) and $SP_{H\text{-}d}$ (diagnosed) are shown on Figure 4 (fourth row, left and right panels, respectively). The $SP_{H\text{-}o}$ field displays positive and negative patterns located in regions where $KE_{igw\text{-}o}$ is large (Figure 3c). The magnitude of $SP_{H\text{-}o}$ is consistent with the magnitude of $KE_{igw\text{-}o}$ and $KE_{g\text{-}o}$. The diagnosed shear production term, $SP_{H\text{-}d}$, (Figure 4, fourth row, right panel) is remarkably similar to the observed one. The correlation between $SP_{H\text{-}d}$ and $SP_{H\text{-}o}$ is close to 0.5 in the Kuroshio Extension and the Agulhas Current but poor for the Drake Passage (Figures S7 and S8). Values of $SP_{H\text{-}o}$ and $SP_{H\text{-}d}$ averaged over the whole domain are close to 10^{-9} m^2/s^3 for the three regions: For instance, in the Kuroshio Extension, the mean value of the shear production estimated from u and v is -1.17×10^{-9} m^2/s^3, and the mean value of the shear production estimated from SSH is -2.5×10^{-9} m^2/s^3. These magnitudes are close to those reported in recent studies although we have applied a double Hanning window on the variables (see section C in supporting information). These results emphasize that SSH observations can help to infer not only the IGWs' spatial organization by BMs but also the energy transfer between these two classes of motions.

One important question is whether KE_{igw} patterns and KE exchanges between IGWs and BMs evolve on a fast time scale (i.e., the propagation time scale of the waves, or ω^{-1}). If the answer is yes, we would need frequent SSH snapshots to monitor IGW-BM interactions. We have performed some sensitivity tests. Although IGW frequencies are larger than f (section B in supporting information), KE_{igw} patterns do not change within 1 or 2 days (cf. Figures 3 and S6). This is true also for the KE exchanges between IGWs and BMs (not shown). Actually, the time evolution of the interactions and KE exchanges appear to follow that of BMs. This means that frequent SSH snapshots are not needed. SSH snapshots with a few days' intervals should be enough to diagnose the spatial organization of IGWs by BMs. This result can be understood within the framework of Young and Jelloul (1997). These authors demonstrated that BMs impact the IGW dispersion on a time scale larger than the IGW oscillating time scale (ω^{-1}) and close to the BMs time scale. Thus,

although u_{igw} and v_{igw} and in particular their direction evolves with a fast time scale, $\mathrm{KE}_{\mathrm{igw}}$ and the KE exchanges between BMs and IGWs evolve only on a slow time scale.

4. Discussion and Perspectives

Recent theoretical and numerical results have emphasized the key role of BM-IGW interactions for the ocean KE budget and therefore for ocean general circulation. These results need to be confirmed by observations in regional or basin-scale domains and over long periods, which is a major challenge. The present study has exploited some spectral properties of BMs and IGWs to understand whether future wide-swath satellite altimeters with high spatial resolution might help to meet this challenge. Although this is a first attempt, results are encouraging and indicate that space observations can help to monitor BM-IGW interactions in the world's oceans. This monitoring will represent a new and major step for our understanding of ocean circulation. There are, however, several caveats to emphasize and some future extensions to mention.

(i) The dynamical framework presented in this study is valid only when the SSH spectrum exhibits a clear slope discontinuity that separates IGWs at small scales from BMs at larger scales. Numerical studies indicate this should be the case in summer in many energetic regions, including the Gulf Stream, the Kuroshio Extension, and the Agulhas Current, where coherent internal tides have a weaker impact on SSH than do BMs (Qiu et al., 2018; Richman et al., 2012; Rocha, Gille, et al., 2016; Torres et al., 2018). But the slope discontinuity still needs to be confirmed by real SSH observations at high spatial resolution, which will be available after SWOT launches in 2021. However, IGWs' dominance in summer, in the small-scale range, has been reported by recent studies using Acoustic Doppler Current Profiler observations. Callies et al. (2015) showed that, in the Gulf Stream recirculation region, IGWs dominate the KE spectrum at scales smaller than 50 km. Qiu et al. (2017) reported similar results in the Kuroshio Extension region. In both studies, the KE spectrum slope in the small-scale range is either similar to, or shallower than, the slope in the larger-scale range. This means that, when using an SSH-KE spectral relationship similar to B8 (section B in supporting information), the resulting SSH spectral slope should be shallower (with a $\kappa^{-2} - \kappa^{-3}$ slope) at smaller scales than at larger scales (usually a $\kappa^{-4} - \kappa^{-5}$ slope), leading to a significant slope discontinuity.

(ii) Our approach, using an LSWM, assumes that IGWs are explained by one dominant baroclinic mode, intimately related to the wave number at which the SSH spectrum exhibits a slope discontinuity. The third baroclinic mode found for the three regions is consistent not only with the findings of Rocha, Gille, et al. (2016) for the Kuroshio Extension but also with the more recent study from Lahaye et al. (2019) for the world ocean in summer. Both studies indicate that the dominance of the third baroclinic mode is explained by shallow mixed layers in summer. Using an LSWM implies a direct relationship between IGW frequencies and wave numbers, that is, $\omega = \omega(\kappa)$, or $\kappa = \kappa(\omega)$. This means all frequencies are supposed to be captured by one spatial snapshot of SSH. Farrar and Durland (2012) relied on a similar relationship $[\omega = \omega(k)]$ to retrieve SSH from mooring data, but considered several baroclinic modes. A future extension of this study should be considering several baroclinic modes by following the approach used in Farrar and Durland (2012).

(iii) Our numerical tests emphasize that IGW-BM interactions involve slow time scale compared with the fast time scales associated with wave frequencies: Within 1 or 2 days, the $\mathrm{KE}_{\mathrm{igw}}$ and SP patterns do not change significantly, meaning that no frequent SSH observations are needed. This slow time evolution can be explained by invoking the linear relationship between IGW frequencies and wave numbers mentioned before. Indeed, considering several wavelengths, as is done when going back to physical space, is equivalent to averaging over different wave periods.

(iv) IGW-BM interactions involving wave numbers $\kappa < K_i$ are not considered in our approach. IGWs at these scales (larger than 50–100 km), which include coherent internal tides and near-inertial waves, represent more than 50% of the total IGW KE in the three regions considered (see also Figure S1). Such IGWs might impact the IGW-BM interactions, in particular, in coastal areas in the presence of a steep topography (Flexas et al., 2015). However, previous studies (Barkan et al., 2017; Rocha et al., 2018; Taylor & Straub, 2016; Thomas, 2017) suggest that it is principally the IGW-BM interactions involving IGW scales smaller than 50–100 km that impact the KE exchanges between IGWs and BMs in energetic regions.

Despite these caveats, results of this study highlight the strong potential of future altimeter missions, such as SWOT, that aim to observe SSH with an unprecedented spatial resolution (~10 km) in two dimensions (wide swath of 120 km) over 68% of the world's ocean. The expected slope discontinuity in the SSH spectrum is such that the small-scale part of the spectrum should be above the noise level, which is likely to be true for high-KE regions of the world's ocean (Wang et al., 2019). SWOT observations will have a repeat period of 21 days. This means interpolation techniques, such as those proposed in Ubelmann et al. (2015), will be needed to produce daily SSH fields. Finally, exploiting the synergy of using SWOT observations with in situ surface drifters will enhance our ability to diagnose BM-IGW interactions in the near future and therefore their impact on the KE budget and ocean general circulation.

References

Alford, M. H., MacKinnon, J. A., Simmons, H. L., & Nash, J. D. (2016). Near-inertial internal gravity waves in the ocean. *Annual Review of Marine Science*, *8*, 95–123. https://doi.org/10.1146/annurev-marine-010814-015746

Arbic, B., Scott, R. B., Flierl, G. R., Morten, A. J., Richman, J. G., & Shriver, J. F. (2012). Nonlinear cascades of surface oceanic geostrophic kinetic energy in the frequency domain. *Journal of Physical Oceanography*, *42*, 1577–1600. https://doi.org/10.1175/JPO-D-11-0151.1

Barkan, R., Winters, K. B., & McWilliams, J. C. (2017). Stimulated imbalance and the enhancement of eddy kinetic energy dissipation by internal waves. *Journal of Physical Oceanography*, *47*, 181–198. https://doi.org/10.1175/jpo-d-16-0117.1

Callies, J., Ferrari, R., Klymak, J. M., & Gula, J. (2015). Seasonality in submesoscale turbulence. *Nature Communications*, *6*(1), 6862. https://doi.org/10.1038/ncomms7862

Danioux, E., Klein, P., & Riviere, P. (2008). Propagation of wind energy into the deep ocean through a fully turbulent mesoscale eddy field. *Journal of Physical Oceanography*, *38*(10), 2224–2241. https://doi.org/10.1175/2008JPO3821.1

Farrar, T. J., & Durland, T. S. (2012). Wavenumber–frequency spectra of inertia–gravity and mixed Rossby–gravity waves in the equatorial Pacific Ocean. *Journal of Physical Oceanography*, *42*(11), 1859–1881. https://doi.org/10.1175/JPO-D-11-0235.1

Ferrari, R., & Wunsch, C. (2009). Ocean circulation kinetic energy: Reservoirs, sources, and sinks. *Annual Review of Fluid Mechanics*, *41*(1), 253–282. https://doi.org/10.1146/annurev.fluid.40.111406.102139

Flexas, M., Schodlok, M. P., Padman, L., Menemenlis, D., & Orsi, A. H. (2015). Role of tides on the formation of the Antarctic slope front at the Weddell-Scotia confluence. *Journal of Geophysical Research: Oceans*, *120*, 3658–3680. https://doi.org/10.1002/2014JC010372

Fu, L.-L., & Ferrari, R. (2008). Observing oceanic submesoscale processes from space. *Eos, Transactions of the American Geophysical Union*, *89*(48), 488. https://doi.org/10.1029/2008EO480003

Klein, P., Lapeyre, G., Siegelman-Charbit, L., Smith, S., Torres, H., & Su, Z. (2019). Ocean scale interactions from space. *Earth and Space Science*, *6*, 795–817. https://doi.org/10.1029/2018EA000492

Kunze, E. (1985). Near-inertial wave propagation in geostrophic shear. *Journal of Physical Oceanography*, *15*(5), 544–565. https://doi.org/10.1175/1520-0485(1985)015<0544:NIWPIG>2.0.CO;2

Lahaye, N., Gula, J., & Roullet, G. (2019). Sea surface signature of internal tides. *Geophysical Research Letters*, *46*(7), 3880–3890. https://doi.org/10.1029/2018GL081848

Polzin, K. L., & Lvov, Y. (2011). Toward regional characterizations of the oceanic internal wavefield. *Reviews of Geophysics*, *49*, RG4003. https://doi.org/10.1029/2010RG000329

Qiu, B., Chen, S., Klein, P., Sasaki, H., & Sasai, Y. (2014). Seasonal mesoscale and submesoscale eddy variability along the North Pacific subtropical countercurrent. *Journal of Physical Oceanography*, *44*, 3079–3098. https://doi.org/10.1175/JPO-D-14-0071.1

Qiu, B., Chen, S., Klein, P., Wang, J., Torres, H., Fu, L.-L., & Menemenlis, D. (2018). Seasonality in transition scale from balanced toun-balanced motions in the world ocean. *Journal of Physical Oceanography*, *48*, 591–605. https://doi.org/10.1175/JPO-D-17-0169.1

Qiu, B., Nakano, T., Chen, S., & Klein, P. (2017). Submesoscale transition from geostrophic flows to internal waves in the northwestern Pacific upper ocean. *Nature Communications*, *8*, 14055. https://doi.org/10.1038/ncomms14055

Richman, J. G., Arbic, B. K., Schriver, J. F., Metzger, E. J., & Wallcraft, A. J. (2012). Inferring dynamics from the wavenumber spectra of an eddying global ocean model with embedded tides. *Journal of Geophysical Research*, *117*, C12012. https://doi.org/10.1029/2012JC008364

Rocha, C. B., Chereskin, T. K., Gille, S. T., & Menemenlis, D. (2016). Mesoscale to submesoscale wavenumber spectra in Drake Passage. *Journal of Physical Oceanography*, *46*, 601–620. https://doi.org/10.1175/JPO-D-15-0087.1

Rocha, C. B., Gille, S. T., Chereskin, T. K., & Menemenlis, D. (2016). Seasonality of submesoscale dynamics in the Kuroshio Extension. *Geophysical Research Letters*, *43*, 11,304–11,311. https://doi.org/10.1002/2016GL071349

Rocha, C. B., Wagner, G. L., & Young, W. R. (2018). Stimulated generation: Extraction of energy from balanced flow by near-inertial waves. *Journal of Fluid Mechanics*, *847*, 417–451. https://doi.org/10.1017/jfm.2018.308

Sasaki, H., Klein, P., Qiu, B., & Sasai, Y. (2014). Impact of oceanic-scale interactions on the seasonal modulation of ocean dynamics by the atmosphere. *Nature Communications*, *5*, 5636. https://doi.org/10.1038/ncomms6636

Taylor, S., & Straub, D. (2016). Forced near-inertial motion and dissipation of low-frequency kinetic energy in a wind-driven channel flow. *Journal of Physical Oceanography*, *46*, 79–93. https://doi.org/10.1175/JPO-D-15-0060.1

Thomas, L. N. (2017). On the modifications of near-inertial waves at fronts: Implications for energy transfer across scales. *Ocean Dynamics*, *67*, 1335–1350. https://doi.org/10.1007/s10236-017-1088-6

Torres, H. S., Klein, P., Menemenlis, D., Qiu, B., Su, Z., Wang, J., et al. (2018). Partitioning ocean motions into balanced motions and internal gravity waves: A modelling study in anticipation of future space missions. *Journal of Geophysical Research: Oceans*, *123*, 8084–8105. https://doi.org/10.1029/2018JC014438

Ubelmann, C., Klein, P., & Fu, L. L. (2015). Dynamic interpolation of sea surface height and potential applications for future high-resolution altimetry mapping. *Journal of Atmospheric and Oceanic Technology*, *32*, 177–184. https://doi.org/10.1175/JTECH-D-14-00152.1

Vallis, G. K. (2017). *Atmospheric and oceanic fluid dynamics*. Cambridge: Cambridge University Press. https://doi.org/10.1017/9781107588417

Wang, J., Fu, L.-L., Torres, H. S., Chen, S., Qiu, B., & Menemenlis, D. (2019). On the spatial scales to be resolved by the surface water and ocean topography KA-band radar interferometer, Accepted in. *Journal of Atmospheric and Oceanic Technology*, *36*, 87–99. https://doi.org/10.1175/JTECH-D-18-0119.1

Whitt, D. B., & Thomas, L. N. (2015). Resonant generation and energetics of wind-forced near-inertial motions in a geostrophic flow. *Journal of Physical Oceanography*, *45*, 181–208. https://doi.org/10.1175/JPO-D-14-0168.1

Young, W., & Jelloul, M. B. (1997). Propagation of near-inertial oscillations through a geostrophic flow. *Journal of Marine Research*, *55*(4), 735–766. https://doi.org/10.1357/0022240973224283